

# Numerical Model of Plasma Sheaths in Hall Thruster

IEPC-2005-12

*Presented at the 29<sup>th</sup> International Electric Propulsion Conference, Princeton University,  
October 31 – November 4, 2005*

F. Taccogna\*

*Max-Planck Institute für Plasmaphysik, EURATOM Association, Wendelsteinstr. 1, Greifswald, D-17491, Germany*

S. Longo<sup>†</sup> and M. Capitelli<sup>‡</sup>

*Dip. Di Chimica, Università degli Studi di Bari, via Orabona 4, Bari, I-70126, Italy*

**Abstract:** The sheath region of a Hall discharge is studied in one spatial (radial in cylindrical metrics) and three velocity dimensions by means of a Particle-in-Cell / Monte Carlo model coupled with a probabilistic method for the secondary electron emission. Different axial regions (anode, ionization and acceleration zones) of the channel have been investigated distinguishing between inner and outer walls. The presheath and sheath structures are different in the three regions simulated showing a charge saturated regime in the acceleration region. Small differences in behaviour for the external and internal walls of the channel are detected. Further, trapped ions are found near the walls in the acceleration region which could have an important effect on the wall recombination enhancing the axial electron current. The results could be used to obtain boundary conditions and lateral wall losses which are suitable for incorporation into models which simulate the bulk neutral plasma.

## Nomenclature

$B$	= magnetic field
$c_s$	= ion sound speed
$E$	= electric field
$I$	= electric current
$k_B$	= Boltzmann constant
$m$	= electron mass
$M$	= Xenon mass
$n$	= number density
$q$	= elementary charge
$T$	= temperature
$v$	= velocity
$\gamma$	= secondary electron emission yield
$\epsilon_0$	= vacuum permittivity
$\Phi$	= electric potential
$\lambda_D$	= Debye length
$\mu$	= electron mobility
$\rho$	= charge density
$\sigma$	= surface charge density and cross section

---

\* PhD, Max-Planck Institute für Plasmaphysik, francesco.taccogna@ba.imip.cnr.it.

<sup>†</sup> Full professor, Dip. Di Chimica, Università degli Studi di Bari, savino.longo@ba.imip.cnr.it.

<sup>‡</sup> Full professor, Dip. Di Chimica, Università degli Studi di Bari, mario.capitelli@ba.imip.cnr.it.

## I. Introduction

Particle and energy losses to the walls are known to affect strongly the Hall thruster performances. A good understanding of the radial plasma-wall interaction is crucial to predict correctly the axial response of the discharge. In particular, the sheath structure inside the acceleration channel is not a classical problem due to a number of mechanisms fairly complicated for different reasons.

First, the potential drops on both the inner and outer sheath and presheath, and, as a result, the electron losses on the channel walls depend strongly on the yield of secondary electron emission (SEE). The use of materials with different SEE to control both the potential profile in a stationary plasma thrusters (SPT), and thereby the efficiency, has been explored theoretically<sup>1</sup> and experimentally<sup>2</sup>. Segmented electrodes made of material with different secondary emission properties have been shown to affect the potential distribution in the SPT channel<sup>3</sup>.

Second, the ion axial and electron azimuthal flows change the structure of the classical sheath reducing the radial losses and increasing the presheath potential drop as already pointed out by Ahedo<sup>4</sup>.

Finally, the interruption of electron drift velocity due to the interaction with a dielectric surface that crosses magnetic field line generates the so called near-wall conductivity (NWC), an important mechanism contributing to the anomalous transport of electron inside the channel<sup>5</sup>.

Up to now, radial models of Hall thrusters have been developed using fluid<sup>4,6</sup> or kinetic-Vlasov<sup>7</sup> approaches. In fluid models, the natural incompatibility between plasma and sheath regions is unsolved and the non-Maxwellian character of primary and secondary electrons is not taken into account. At the same time, the kinetic work of Morozov and Savel'ev<sup>7</sup> neglects plasma flow, collisional and magnetic field effects. Moreover, in their work, the surface is not allowed to float. Finally, a lot of axial models<sup>8-15</sup> have also been developed where the radial effects are included in one-dimensional equations. However, they use quasineutrality hypothesis in the computation of the electric potential. This produces the inconvenient that computation domain does not end at the thrusters walls but at the transition to the quasineutral presheaths. For this reasons, these models need to solve sheaths separately and to substitute wall conditions by sheath transition conditions. Finally, very often, results are possible only with the use of corrections to various transport and energy parameters and these corrections are not rigorously defined by the actual physics governing these processes.

The objective of this work is to provide a better understanding of the radial behaviours inside the Hall thruster SPT-100. For this purpose, a radial cylindrical 1D(r)-3V fully kinetic Particle-in-Cell / Monte Carlo Collision (PIC/MCC)<sup>16,17</sup> model of the presheath, transition layer and sheath including electron-neutral collisions and the process of secondary electron emission from the dielectric walls has been developed. The "local-field approximation" is used simulating different axial sections (anode, ionization and acceleration regions) neglecting the effects of axial gradients on the basis of the fact that all the axial gradient length are greater than the characteristic lengths of the system and the radial gradient length.

## II. Theory

### A. Role of SEE

When secondary electron emission from the wall is allowed for, the potential jump in the collector sheath is reduced. The behaviour of the potential remains monotonic until the secondary emission coefficient  $\gamma$  reaches a critical value  $\gamma_c$  or equivalently the effective secondary electron emission coefficient  $\Gamma$  integrated over the impinging electron distribution function approaches unity. At this point, a zero electric field at the emitter occurs (field reversal point). Using a fluid approach<sup>18</sup>, assuming the electron distribution function to be Maxwellian, the voltage drop  $\Delta\phi_s$  through the sheath is given by:

$$\Delta\phi_s = -\frac{k_B T_e}{q} \ln \left[ (1 - \Gamma) \sqrt{\frac{M}{2\pi m}} \right] \quad (1)$$

For  $\gamma > \gamma_c$  kinetic models<sup>19,20</sup> have showed that the classical Debye layer disappears and transforms into a non-monotonic double layer structure. A potential well forms close to the wall which traps a fraction of the secondary electrons. This charge saturated regime (CSR) is characterized by a constant  $\gamma_{CSR}$  and a sheath potential done respectively by:

$$\Gamma_{CSR} \approx 1 - 8.3 \sqrt{\frac{m}{M}} \quad (0.983 \text{ for Xe}) \quad (2.a)$$

$$\Delta\phi_{s,CSR} \approx \frac{k_B T_e}{q} \ln \left[ (1 - \Gamma_{CSR}) \frac{1}{\sqrt{2\pi}} \frac{v_{e,th}}{c_s} \right] \quad (2.b)$$

while the potential dip generating in front of the collector surface is done by

$$\Delta\phi_w = \frac{k_B T_{e,s}}{q} \ln \left( \frac{\Gamma}{\Gamma_{CSR}} \right) \quad (2.c)$$

Under such conditions, the channel wall acts as an extremely effective energy sink, which tends to limit the electron temperature.

However, in SPT the picture becomes much more complex. First, the distribution functions of electrons hitting the surface and secondary electrons emitted from the walls are essentially non-Maxwellian. It has been proofed<sup>17</sup> that in this case the electron temperature limitation occurs at a rather high level. Indeed, due to electron attachment to the walls, wall collisions depopulate the tail of the electron distribution function, thus strongly reducing the effective SEE coefficient and energy losses on the wall. Space-charge saturation of the wall sheath might be achieved at a higher mean energy of the electron distribution function bulk, than predicted by a simple averaging over the Maxwellian.

Second, the electrons in the SPT have energies in the range of 15-30 eV (necessary to ionize Xenon) and most of the ceramics used to made the thruster walls are characterized by a relatively high value of secondary electron emission coefficient at these energies. Moreover, for high electron temperature, it has been shown<sup>6</sup> that the sheath loses its static character becoming a structure oscillating in space and time extended in a region with size  $L \gg \lambda_D$ .

## B. Near wall conductivity

Another effect of electron-wall interaction is the enhanced electron axial conductivity. It has been suggested that a large fraction of electron diffusion across the radial magnetic field lines is due to the so-called near-wall conductivity based on the electron collisions with the walls that nullify the mean momentum of re-emitted electrons. Indeed, the small value of the potential difference at the plasma sheath on the walls for high secondary electron emission coefficient (Eqs. (2)), leads to a large number of electrons reaching the surfaces.

An incoming electron follows a spiral trajectory due to the magnetic field, collides with the walls and leaves following another spiral trajectory, which is usually displaced toward a more positive potential, against  $\mathbf{E}$ . This mechanism known as diffusive near-wall conductivity leads to the Morozov's formula<sup>10</sup> for the axial electron mobility:

$$\mu = \frac{2m v_{e,th}}{q(R_{out} - R_{in})B^2} \quad (3.a)$$

The secondary electron emission mechanism was not included in Morozov's works. Taking into account the effective secondary electron emission yield, the near-wall mobility becomes<sup>21</sup>:

$$\mu = \frac{2m c_s}{q(R_{out} - R_{in})B^2} \frac{\Gamma}{1 - \Gamma} \quad (3.b)$$

### III. Numerical Model

#### A. Bulk plasma phase: PIC-MCC Model

The simulation has been done per unit of transverse length. Each computational particle represents a charge per unit of length. Motion and collisions of macroparticles can be treated separately by the principle of decoupling if a chosen timestep gives a small collision probability. The simulation region is initially empty. A planar source model is used to inject the particles (electrons and ions) with a half-Maxwellian velocity distribution inside the simulated region. The Buneman-Boris version of the leapfrog method<sup>17</sup> is used to integrate the equation of motion for a simulated particle. Once the new positions are obtained for all charged particles, the charge density  $\rho$  is determined from the Verboncoeur charge assignment rule<sup>22</sup> (which guarantees density conservation on a radial metrics) on a computational grid and the Poisson equation:

$$\left( \frac{\partial^2}{\partial r^2} + \frac{1}{r} \frac{\partial}{\partial r} \right) \phi(r) = -\frac{\rho(r)}{\epsilon_0} \quad (4)$$

is discretized and solved iteratively using a SOR technique with Chebyshev acceleration<sup>16</sup>. For this purpose, a fixed Dirichlet boundary condition is used at the plasma source with  $E_r=0$ , while the plasma-facing material surface can electrically float respect to the plasma such that the total current density to the surface is zero (zero-current condition). The collector potential is calculated each timestep assuming a linear characteristic response of the material:

$$\phi_w^{(n+1)} = \phi_w^{(n)} + C(I_i - I_e) \quad (5)$$

(the value of the coefficient C is equal to  $5 \times 10^{-4}$  V/A for the material studied), while the electric field at the wall is proportional to the net charge  $\sigma_w$  that has accumulated on the surface (the possible surface conductivity of the dielectric is neglected):

$$E_r = -\frac{\sigma_w}{2\epsilon_0} \quad (6.a)$$

$$E_z = 0 \quad (6.b)$$

The radial component of the magnetic field is written as

$$B_r(r) = B_0 \frac{r_0}{r} \quad (7)$$

As regards collisions, we consider electron-neutral interaction using Monte Carlo method. Elastic scattering, excitation and first ionization are treated. Only one excitation collision has been considered. Anyway, the excited states kinetics is not included, considering the quenching of excited states instantaneous. For the MCC algorithm, we assume the neutrals as infinitely heavy, and therefore the neutral velocity is neglected compared to the electron one. For each electron, we calculate the probability of an e-N scattering  $P_{tot}$  during the timestep  $\Delta t$ :

$$P_{tot} = n_N \sigma_{tot}(v_e) v_e \Delta t = \sum_{k=1}^3 n_N \sigma_k(v_e) v_e \Delta t = \sum_{k=1}^3 P_k \quad (8.a)$$

where  $n_N$  is the neutral density,  $\sigma_{tot}$  is the total electron-neutral cross section,  $v_e$  is the electron velocity and  $P_1$ ,  $P_2$  and  $P_3$  are the probability for the occurrence of collisional event 1, 2, and 3, respectively.  $P_{tot}$  is compared with a random number  $r_d$  sampled from an uniform distribution in the range [0,1] in order to decide if a collision event happens (in our case  $\Delta t$  is chosen so that  $P_{tot} < 10^{-2}$ ). If  $P_{tot} > r_d$ , we compare another random number to the cross

sections for elastic scattering, excitation, and ionization to determine which type of event occurs. We choose the collisional event  $j$  if

$$\sum_{k=1}^{j-1} \frac{P_k}{P_{tot}} < r_d \leq \sum_{k=1}^j \frac{P_k}{P_{tot}} \quad (8.b)$$

In all cases, the electron is scattered isotropically. If collision is inelastic, energy (8.32 eV for the first excitation and 12.1 eV for the first ionization) is subtracted from the electrons. In the case of ionization, ions and secondary electrons are created at the primary electron's location. The energy of primary and secondary electrons is divided randomly, while the initial ion velocity is set from a Maxwellian distribution at the neutral temperature.

### B. Secondary electron emission model

The two main quantities used to study the secondary emission process are the secondary-emission yield (SEY)  $\gamma(E_p)$  and the emitted energy spectrum  $d\gamma/dE$ .

The typical dependence of  $\gamma$  from the kinetic energy  $E_p$  of the incident electron beam is shown in Fig. 1 for BN. It increases with  $E_p$  in the low-energy region, reaches a maximum value, and then decreases with increasing primary energy. Moreover, it has been observed that for a given primary energy, SEY increases with increasing angle of incidence  $\theta$  measured relative to the surface normal due to the production of secondary electrons closer to the surface.

As regard the energy distribution function, analyzing the spectra of electrons coming from a surface (see Fig. 2), we can observe three different phenomena:

- the peak marked with (a) corresponds to electrons scattered elastically from the surfaces with energy slightly below the incident energy;
- the small peak marked (b) is due to electrons that suffer inelastic scattering;
- the peak (c) corresponds to secondary electrons with low energy (<10 eV).

As a consequence, the total yield can be considered as the sum of these three contributions:

$$\gamma_{tot}(E_p) = \gamma_e(E_p) + \gamma_r(E_p) + \gamma_{ts}(E_p) \equiv \frac{I_e}{I_0} + \frac{I_r}{I_0} + \frac{I_{ts}}{I_0} \quad (9)$$

This distinction is important in order to understand the behaviour of SEY at low primary energy (<20 eV). It is well documented<sup>23,24</sup> that the fraction of electrons backscattered is dominant at energies typical for SPT operation. It has been shown that the backscattering coefficient ( $\gamma_e + \gamma_r$ ) is usually growing with the decrease of  $E_p$ , while the yield of true secondary electrons  $\gamma_{ts}$  decreases and reaches zero at an energy of about the width of the potential gap between vacuum and the upper level of the valence band.

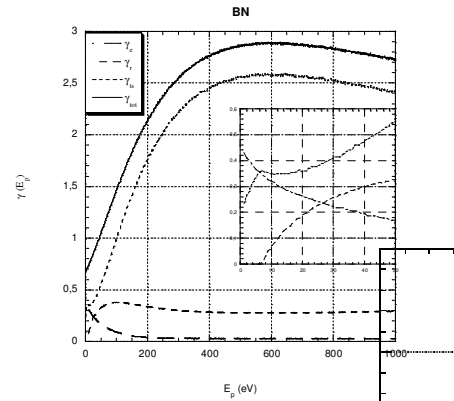


**Figure 1. Dependence of  $\gamma$  on the incident electron energy for BN as material calculated in the model.**

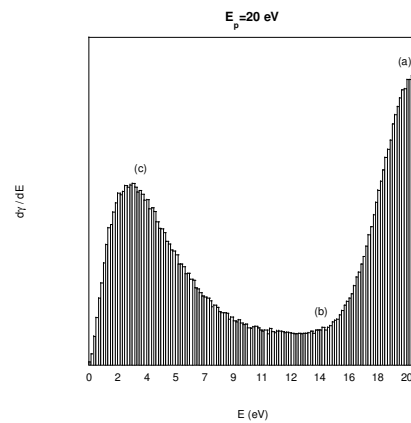


**Figure 2. Energy distribution of electron emitted from a BN bombarded with 20 eV electrons.**

To model the secondary-emission process we have implemented the Monte Carlo phenomenological model of Furman and Pivi<sup>25</sup>. It is based on the construction of a set of probabilities for the generation of secondary electrons given the primary electron energy and angle, by using a number of parameters fitting measured data<sup>26</sup> as the secondary emission yield and the emitted energy spectrum of secondary electrons. The reader is remanded to Ref. 25, 27 and 28 for a detailed description of the entire implementation.

## IV. Results and Discussion

### A. Radial structure of sheaths

In Figs. 3 and 4, the radial profiles in the steady-state conditions are shown for the three different regions in the outer and inner walls, using BN as material. In these figures, the inner wall is placed on the left hand side and the outer wall on the right hand side. The profiles are averaged values of 200 time steps.

The potential profiles are given in Figs. 3, where the inserts detail the sheath regions.

The build-up of a large negative potential drop and corresponding repulsive electric field from the walls is present in the anode and ionization regions, while a charge saturated regime appears in the acceleration region with a double-layer structure. The sheath drop decreases from the anode to the acceleration regions, whereas the potential drop in the presheath, not negligible at all, as already observed by Ahedo<sup>4</sup>, it increases from the anode to the acceleration regions. Generally, the potential drop in the presheaths are larger than in the sheaths.

It is impossible to define a sheath edge in the acceleration region due to the presence of a space saturated regime. Here, the behaviour of electric potential is not more monotonic and potential dips  $\Delta\phi_w$  in front of the walls appear equal to 0.12 V and 0.21 V for the inner and outer walls respectively. This creates a reversed radial electric field  $E_{r,w}$  on the wall equal to 11031 V/m and -11384 V/m for the inner and outer walls respectively.

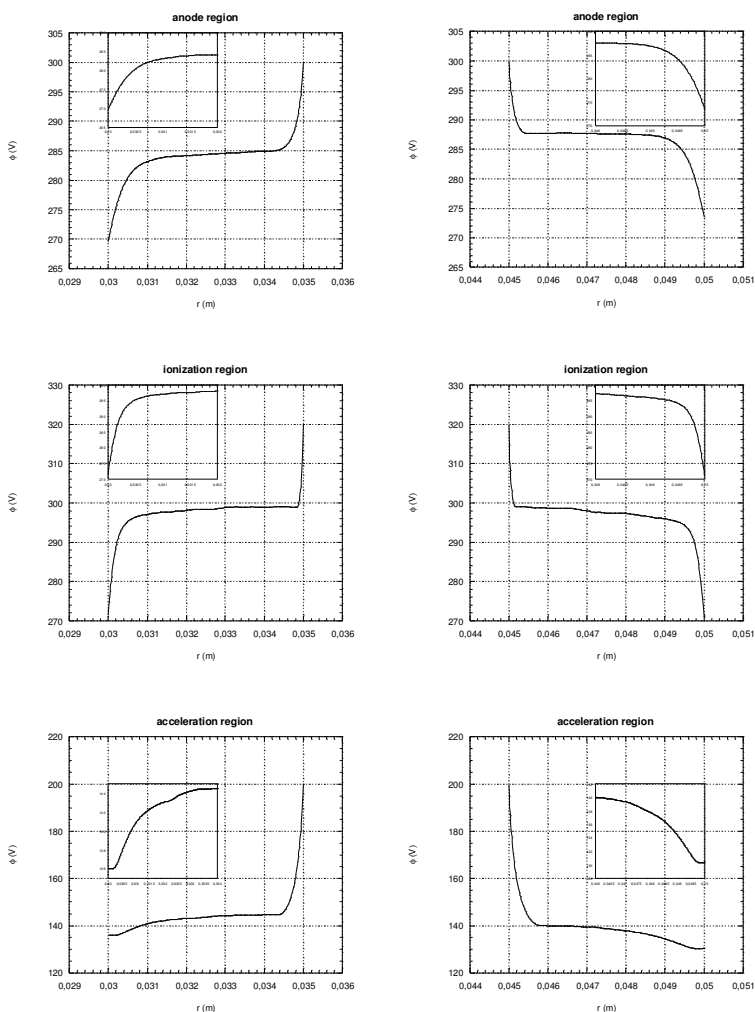


**Figure 3. Radial profiles of the electric potential in the different regions of the channel. The inner wall is placed on the left-hand side and the outer wall on the right-hand side. The inserts detail the sheath.**

In Figs. 4, ion and electron (primary and secondary) density are plotted. We distinguish in all the three regions the presheath, the quasineutral transition layer (where electron and ion densities are comparable) and the sheath (primary electron density negligible). It is evident the presence of the unexpected breaking of electric neutrality at  $r=0.035$  m and  $r=0.045$  m, resulting from the applied procedure of replacing the large presheath by a narrow source sheath. As previously pointed out this effect does not affect the general sheath structure. Due to negative potential build-up on the wall in the anode and ionization regions, electrons are repelled and their number density decreases rapidly whereas, decrease in ion number density is gradual. This is consistent with the classical sheath picture near the wall. The situation is different in the acceleration region, where the CSR causes an increment of the secondary electron density near the wall with the presence of an electron sheath.

The profiles of the inner and outer regions are asymmetrical in the anode and acceleration regions: larger potential drops are found in the inner anode and outer acceleration zones.

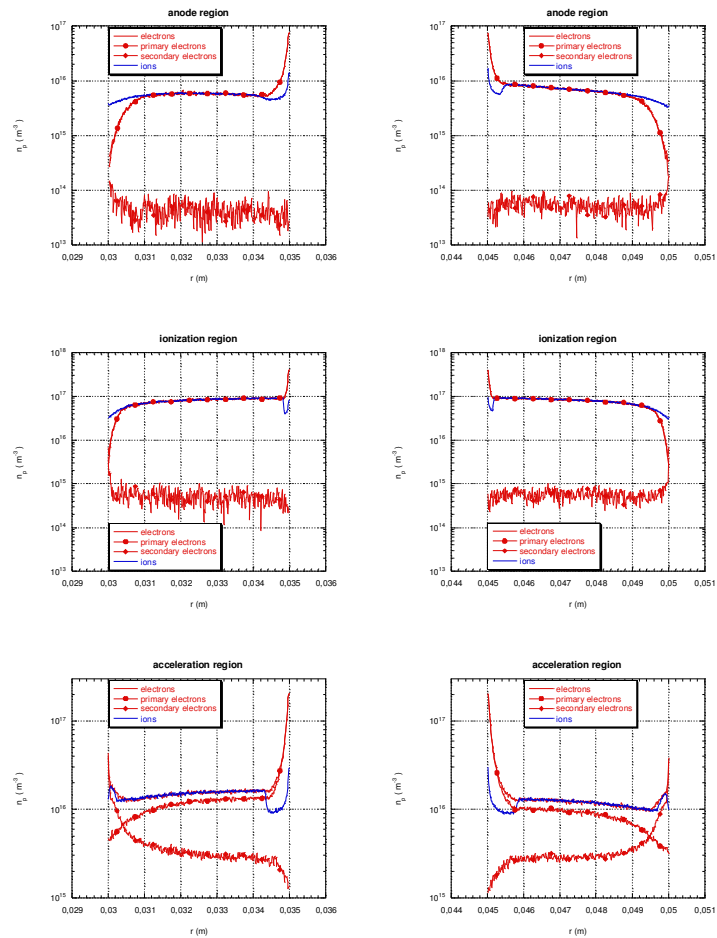


**Figure 4. Radial profiles of the electron (primary and secondary) and ion density in the different regions of the channel.**

The relevant role of secondary electrons in the acceleration region is confirmed by the plot reported in Fig. 5. It is shown the electron velocity distribution  $f(v_e)$  in the three different regions of the outer wall. It can be easily seen the presence of a beam-like secondary electrons characterized by a negative radial velocity much less prominent in the anode and ionization regions.

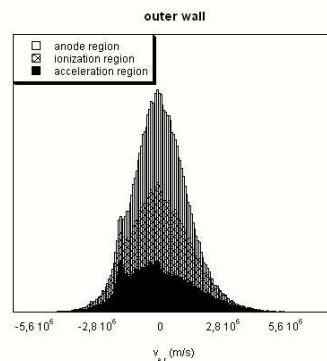


**Figure 5. Electron velocity distribution in the different axial regions for the outer wall.**

As regard the investigation of the ion kinetic behaviour, the phase-space distribution reported in Figs. 6 for the inner wall, shows the presence of two families of ions in all the regions, a beam-like and a thermal one produced by ionization processes. It is quite interesting to note a presence of trapped ions in the potential well of the acceleration region. These ions could play an important role concerning the electron-ion wall recombination. This mechanism has been proposed to explain the enhanced axial electron current by volume ionization of neutrals emitted from the walls<sup>29</sup>.

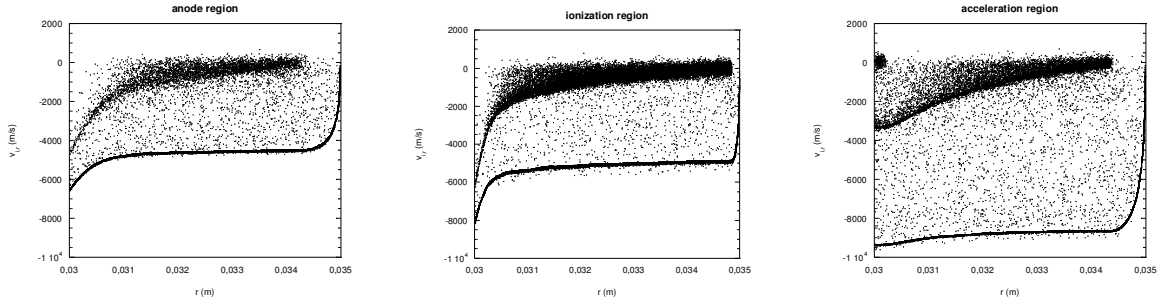


**Figure 6. Phase space distribution of electrons in the different axial regions for the outer wall.**

### B. Near wall conductivity

In Figs. 7 the radial profile of the axial electron velocity is depicted for the three different regions in the inner and outer walls.

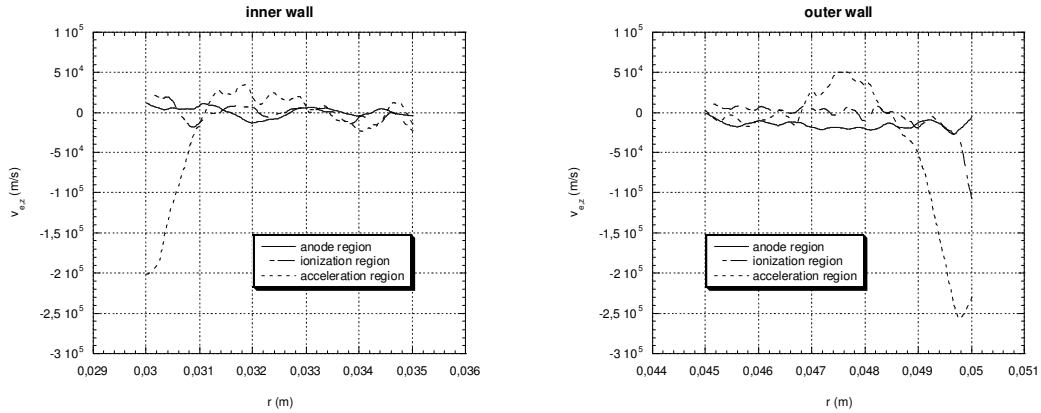


**Figure 7. Radial profiles of the axial electron velocity in the different regions of the channel.**

The appearance of an oscillatory structure in the radial profile of axial current is the characteristic signature of near-wall conductivity, which distinguishes it from the classical bulk conductivity transverse to the magnetic field. These profiles can be interpreted as follows: secondary electrons initially tend to move against  $\mathbf{E}$  due to electrostatic force, but become as soon involved in a cycloidal motion due to the magnetic field and their axial velocity  $v_z$  thus changes along the radial direction as  $\sin(\omega_{ce}t/v_r)$ . Due to the randomness of the initial velocities  $v_r$ , the phase  $\psi = \omega_{ce}t/v_r$  of the different electrons become uncorrelated away from the walls and their respective contributions to the main axial velocity eventually cancel. When the sheath potential is larger than the velocity dispersion, however, the distribution of velocities  $v_r$  becomes confined close to  $v_r = \sqrt{2q\Delta\phi_s/m}$  which results in a better correlation of the phases, even relatively far from the wall. The spatial period is proportional to  $\sqrt{\Delta\phi_s/k_B T_{e,s}}$  and the amplitude of the near wall current is characterized by a decay in  $r^{-1}$  for large  $r$ . This behaviour is confirmed in Figs. 7. The wall conduction

layer is most pronounced near the outer wall of the channel and it is less defined near the inner ceramic. Moreover, no strong oscillations of the axial electron velocity near the inner walls of the channel are observed. The most likely reason for this difference in behaviour of  $v_{e,z}(r)$  near the external and internal walls of the channel is the greater sheath drop and magnetic field in the outer part, and also an annular effect. Indeed, as demonstrated by a recent Monte Carlo simulation<sup>30</sup>, the ratio of the velocity peaks is approximately the same as the ratio of the inner and outer radii:

$$\frac{\Delta v_{e,z,in}}{\Delta v_{e,z,out}} = \frac{R_{in}}{R_{out}} \quad (10)$$

as a consequence of the behaviour of the radial component of the magnetic field.

## V. Conclusion

A 1D(r)-3V PIC-MCC model was developed to assess the effect of dielectric walls in stationary plasma thrusters. The emission of secondary electron by electron impact from the walls is taken into account by a probabilistic model simulating the different kind of electrons created at the wall, backscattered, rediffused and true secondaries. Different axial regions (anode, ionization and acceleration zones) of the channel have been investigated using the local field approximation and distinguishing between inner and outer walls. The major results include the presence of a charge saturated regime with associated near wall conductivity and trapped ions in the accelerated region, while the sheaths in the anode and ionization regions have a standard behaviour.

## Acknowledgments

This work is supported by the European Community under the MARIE CURIE INTRA-EUROPEAN FELLOWSHIP: "Negative ion source model".

## References

- <sup>1</sup>Fruchtman, A., Fish, N. J., and Raitses, Y., "Control of the electric-field profile in the Hall thruster", *Phys. Plasmas*, Vol. 8, No. 3, 2001, pp. 1048-1056.
- <sup>2</sup>Raitses, Y., Dorf, L. A., Litvak, A. A. and Fish, N. J., "Plume reduction in segmented electrode Hall thruster", *J. Appl. Phys.*, Vol. 88, No. 3, 2000, pp. 1263-1270.
- <sup>3</sup>Raitses, Y., Keidar, M., Staack, D., and Fish, N. J., "Effects of segmented electrode in Hall current plasma thrusters", *J. Appl. Phys.*, Vol. 92, No. 2, 2002, pp. 4906-4911.
- <sup>4</sup>Ahedo, E., "Presheath/sheath model with secondary electron emission from two parallel walls", *Phys. Plasmas*, Vol. 9, N. 10, 2002, pp. 4340-4347.
- <sup>5</sup>Morozov, A. I., "Effect of near-wall conductivity in a strongly magnetized plasma", *Zh. Prikl. Mekh. Tekh. Fiz.*, Vol. 3, 1968, pp. 19 (in Russian).
- <sup>6</sup>Roy, S., Pandey, B. P., Poggie, J., and Gaitonde, D. V., "Modeling low pressure collisional plasma sheath with space-charge effect", *Phys. Plasmas*, Vol. 10, N. 6, 2003, pp. 2578-2585.
- <sup>7</sup>Morozov, A. I., and Savel'ev, V. V., "One-dimensional model of the Debye layer near a dielectric surface", *Plasma Phys. Rep.*, Vol. 28, No. 12, 2002, pp. 1103-1109.
- <sup>8</sup>Fife, J. M., "Hybrid-PIC modeling and electrostatic probe survey of Hall thruster", Ph.D. thesis, Massachusetts Institute of Technology, Boston, MA, 1999.
- <sup>9</sup>Choueiri, E. Y., "Fundamental difference between the two Hall thruster variants", *Phys. Plasmas*, Vol. 8, No. 11, 2001, pp. 5025-5033.
- <sup>10</sup>Keidar, M., Boyd, I. D., and Beilis, I. I., "Plasma flow and plasma-wall transition in Hall thruster channel", *Phys. Plasmas*, Vol. 8, No. 12, 2001, pp. 5315-5322.
- <sup>11</sup>Roy, S., and Pandey, B. P., "Plasma-wall interaction inside a Hall thruster", *J. Plasma Phys.*, Vol. 68, No. 4, 2002, pp. 305-319.
- <sup>12</sup>Meezan, N. B., and Cappelli, M. A., "Wall material effects in stationary plasma thrusters. II. Near-wall and in-wall conductivity", *Phys. Rev. E*, Vol. 66, 2002, 036401.
- <sup>13</sup>Ahedo, E., Gallardo, J. M., and Martinez-Sánchez, M., "Kinetic study of wall collisions in a coaxial Hall discharge", *Phys. Plasmas*, Vol. 10, No. 8, 2003, pp. 3397-3409.
- <sup>14</sup>Dorf, L., Semenov, V., and Raitses, Y., "Anode sheath in Hall thrusters", *Appl. Phys. Lett.*, Vol. 83, No. 13, 2003, pp. 2551-2553.

- <sup>15</sup>Barral, S., Makowski, K., Peradzyński, Z., Gascon, N., and Dudeck, M., “Wall material effects in stationary plasma thrusters. II. Near-wall and in-wall conductivity”, *Phys. Plasmas*, Vol. 10, No. 10 2003, pp. 4137-4152.
- <sup>16</sup>Eastwood, J. W., and Hockney, R. W., *Computer Simulation Using Particle*, McGraw-Hill, New York, 1981.
- <sup>17</sup>Birdsall, C. K., and Langdon, A. B., *Plasma Physics via Computer Simulation*, McGraw-Hill, New York, 1985.
- <sup>18</sup>Hobbes, G. D., and Wesson, J. A., “Heat flow through a Langmuir sheath in the presence of electron emission”, *Plasma Phys.*, Vol. 9, 1967, pp. 85-87.
- <sup>19</sup>Schwager, L. A., “Effects of secondary and thermionic electron emission on the collector and source sheaths of a finite ion temperature plasma using kinetic theory and numerical simulation”, *Phys. Fluids B*, Vol. 5, No. 2, 1993, pp. 631-645.
- <sup>20</sup>Taccogna, F., Longo, S., and Capitelli, M., “Plasma-surface interaction model with secondary electron emission effects”, *Phys. Plasmas*, Vol. 11, No. 3, 2004, pp. 1220-1228.
- <sup>21</sup>Gascon, N., Dudeck, M., and Barral, S., *Phys. Plasmas*, “Wall material effects in stationary plasma thrusters. I. Parametric studies of an SPT-100”, Vol. 10, No. 10, 2003, pp. 4123-4136.
- <sup>22</sup>Verboncoeur, J. P., “Symmetric spline weighting for charge and current density in particle simulation”, *J. Comput. Phys.*, Vol. 174, 2001, pp. 421-427.
- <sup>23</sup>Fridrikhov, S. A., and Shul'man, A. R., “An investigation of secondary electron emission by certain dielectrics at low primary electron energies”, *Sov. Phys. Solid State*, Vol. 1, 1959, pp. 1153-1159.
- <sup>24</sup>Bazhanova, N. P., Belevskii, V. P., and Fridrikhov, S. A., “Secondary electron emission from barium oxide and yttrium oxide due to low-energy primary electrons (1-100 eV)”, *Sov. Phys. Solid State*, Vol. 3, No. 9, 1962, pp. 1899-1905.
- <sup>25</sup>Furman, M. A., and Pivi, M. T. F., “Probabilistic model for the simulation of secondary electron emission”, *Phys. Rev. ST Accel. Beams*, Vol. 5, No. 12, 2002, 124404.
- <sup>26</sup>Viel-Inguibert, V., “Secondary electron emission of ceramics used in the channel of SPT”, *Proceedings of the 28<sup>th</sup> International Electric Propulsion Conference, Toulouse 2003*, Electric Rocket Propulsion Society, Cleveland, OH, 2003, IEPC-2003-258.
- <sup>27</sup>Taccogna, F., “Plasma-surface interaction inside a Hall thruster”, Ph.D. thesis, Universita' degli Studi di Bari, Bari, Italy, 2003.
- <sup>28</sup>Taccogna, F., Longo, S., and Capitelli, M., “Plasma sheaths in Hall discharge”, *Phys. Plasmas*, Vol. 12, 2005, 093506.
- <sup>29</sup>Ivanov, A. A., Ivanov, A. A. Jr., and Bacal, M., “Effect of plasma-wall recombination on the conductivity in Hall thrusters”, *Plasma Phys. Contr. Fus.*, Vol. 44, 2002, pp. 1463-1470.
- <sup>30</sup>Yu, D. R., Wu, Z. W., and Wang, X. G., “Numerical simulation for near wall conductivity effect on current profiles in the annular channel of Hall-type stationary plasma thrusters”, *Phys. Plasmas*, Vol. 12, 2005, 043507.